LANGMUIR

pubs.acs.org/Langmuir Article

Generating Stable Nitrogen Bubble Layers on Poly(methyl methacrylate) Films by Photolysis of 2-Azidoanthracene

Pranaya P. Ghate, Kerry M. Hanson, Kevin Lam, Rabih O. Al-Kaysi, and Christopher J. Bardeen*



Cite This: *Langmuir* 2024, 40, 4054–4062



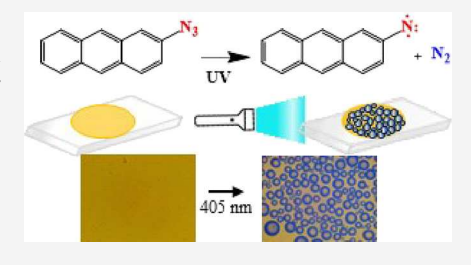
ACCESS

III Metrics & More

Article Recommendations

SI Supporting Information

ABSTRACT: 2-Azidoanthracene ($2N_3$ -AN) can act as a photochemical source of N_2 gas when dissolved in an optically transparent polymer such as poly(methyl methacrylate) (PMMA). Irradiation at 365 or 405 nm of a 150 μ m-thick polymer film submerged in water causes the rapid appearance of a surface layer of bubbles. The rapid appearance of surface bubbles cannot be explained by normal diffusion of N_2 through the polymer and likely results from internal gas pressure buildup during the reaction. For an azide concentration of 0.1 M and a light intensity of 140 mW/cm², the yield of gas bubbles is calculated to be approximately 40%. The dynamics of bubble growth depend on the surface morphology, light intensity, and $2N_3$ -AN concentration.



A combination of nanoscale surface roughness, high azide concentration, and high light intensity is required to attain the threshold N_2 gas density necessary for rapid, high-yield bubble formation. The N_2 bubbles adhered to the PMMA surface and survived for days under water. The ability to generate stable gas bubbles "on demand" using light permits the demonstration of photoinduced flotation and patterned bubble arrays.

INTRODUCTION

Stimuli-responsive polymers have applications across a wide range of fields from medicine to engineering to soft robotics.³ The response of the polymer can involve changes in its chemical properties, for example, a pH change, or its physical properties, such as its volume. To generate large and discontinuous changes in physical properties such as the volume or elastic modulus, a common strategy is to create a new phase of matter that is contained within or attached to the solid. One example is the order-disorder transition in liquid crystal elastomers that drives morphology changes in response to heat or light.^{4,5} Alternatively, the new phase can arise due to molecular species embedded in the polymer. For example, the solid-to-liquid phase transition of organic molecules has been harnessed for heat storage,6 actuation,7,8 and switchable adhesion. The large volume expansion associated with a liquid-to-gas transition is the basis for a class of polymer actuators. 10-13 To generate a response that relies on generating a new phase of matter, light is a useful stimulus because it does not require physical contact and has a wide range of parameters (wavelength, intensity, and duration) that can be manipulated to elicit the desired response.

Photoinduced solid \rightarrow gas transitions in polymers have received little attention in the context of stimuli-responsive materials. This is probably because direct sublimation of a solid usually requires a low pressure or high temperature and is rarely observed under ambient conditions. In order to generate gas from solids, chemical mechanisms are typically preferred with the rapid thermal decomposition of NaN₃ or guanidine nitrate in automobile airbags being one widely utilized example. A controlled way to initiate gas evolution from a

solid could have beneficial applications beyond airbags especially in liquid environments. For example, the ability to create gas bubbles from a solid object "on demand" could be used for propulsion or to modify fluid flow, heat transfer, or acoustic wave propagation. There exist many organic photocleavage reactions that generate gases such as N₂, CO₂, or CO as products. ¹⁵ N₂ can be produced by photodecomposition of azridines, ¹⁶ but the azide photolysis reaction in particular has been more studied ^{17–19} because it gives rise to reactive nitrene species. ²⁰ In most of these studies, N₂ is a byproduct that is assumed to diffuse away as it dissolves in solution. However, if N₂ gas evolution from a solid film could be made sufficiently rapid as recently observed in azide molecular crystals, ²¹ the N₂ molecules can nucleate into bubbles, trapping the gas in a more useful form and creating a new type of photoresponsive material.

In this paper, we utilize the molecule 2-azidoanthracene $(2N_3$ -AN) as a photoreactive source of N_2 gas generation. In solution under near-ultraviolet (UV) light, this molecule undergoes photolysis to form nitrene side products that absorb across the visible spectrum without the creation of stable bubbles. When this molecule was dissolved in the optically transparent polymer poly(methyl methacrylate) (PMMA),

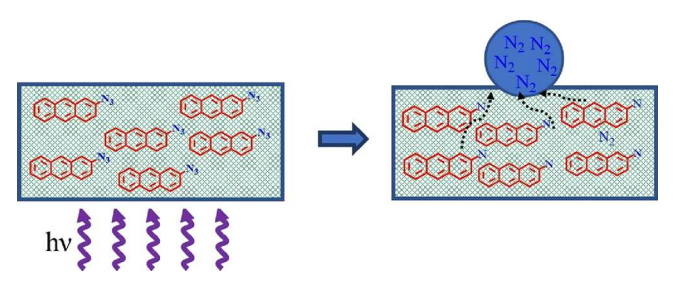
Received: September 22, 2023 Revised: January 22, 2024 Accepted: January 23, 2024 Published: February 14, 2024





similar photochemistry is observed, but the evolved N_2 gas diffuses to the surface of the polymer film where it nucleates into a stable layer of bubbles. This process is outlined in Scheme 1. The dynamics of bubble growth are found to

Scheme 1. How Irradiation of Aromatic Azide (red) Embedded in the Polymer (green) Gives Rise to N_2 Bubbles at the Surface



depend on the surface morphology, light intensity, and $2N_3$ -AN concentration. Rapid bubble formation requires a combination of a textured surface, high azide concentrations, and high light intensities in order to attain efficient bubble formation. The ability to generate N_2 bubbles "on demand" using light is used to demonstrate patterned arrays of bubbles and photoinduced flotation of objects. Photochemical surface bubble formation may provide a convenient and general way to modulate material properties, such as the surface drag, ^{22,23} acoustic wave propagation, ^{24–26} ultrasound contrast, ²⁷ strain in 2D materials, ²⁸ thermal transport, ²⁹ and buoyancy. ³⁰

EXPERIMENTAL SECTION

Sample Preparation. The synthesis and characterization of 2-azidoanthracene $(2N_3$ -AN) have been reported previously. The detailed synthesis and characterization are described in the Supporting Information. To prepare polymer films, $2N_3$ -AN was dissolved in HPLC-grade chloroform (Fisher Scientific) under low-light conditions. The resulting stock solution was mixed with poly(methyl methacrylate) (PMMA; Sigma-Aldrich, average molecular weight ~120,000) to achieve the desired azide concentration. The PMMA solution was drop-cast onto glass slides that had been rinsed with acetone and air-dried. The polymer solution was added in the center of a 1 in. diameter glass cylinder resting on top of the slide, which limited spreading and ensured a reproducible film diameter and thickness. Once enough chloroform had evaporated to render the mixture viscous, the glass cylinder was removed, and the films were left to dry for 12 h in the open air but protected from light exposure.

Rapid solvent evaporation led to a hazy appearance of these "rough" films. To protect the sample from ambient air currents and slow down evaporation, a closed glass container was placed over the sample on a lab bench. After drying overnight, these "smooth" films were noticeably more homogeneous than those left to dry in open air as judged by the absence of optical scattering.

Film Characterization. The film thicknesses were measured to be $150 \pm 20~\mu m$ using a Mitutoyo 543-793-10 ID-S112TX Digimatic Indicator. Static contact angle measurements were performed on a Biolin Scientific Theta Flex optical tensiometer using the sessile drop method. For the air—water—PMMA interface measurements, a drop size of $5~\mu L$ was used. For the water/N₂/PMMA measurements, a square piece of the $2N_3$ -AN polymer film was placed in a 1 cm path length quartz cell cuvette, submerged in deionized water, and then irradiated with 365 nm light from an AloneFire SV-13 UV light source for $5~\min$. Raman characterization was conducted using a Horiba LabRam/Aist-NT AFM with a $100\times$ objective and 532~nm laser excitation source.

Microscopy. To image bubble formation, a glass slide with a PMMA film was suspended in a water-filled Petri dish with the polymer side facing down. An Olympus IX70 inverted microscope with a 4× objective was used to image the sample, while filtered light from a Hg lamp excited the sample at either 365 or 405 nm. The intensity was measured with a Vega (P/N 7Z01560) power meter attached to a 10 mm diameter circular laser sensor that measured up to 3 W. The excitation light intensity was attenuated with glass neutral density filters (ThorLabs). An AMScope MU1000 digital camera was used to record the photochemical bubble evolution. All experiments were conducted at room temperature and atmospheric pressure. For all experiments, the PMMA film weight was 0.1% of the water mass added to the glass dish; therefore, water was present in excess. The light irradiation area was 0.7 cm² on a 4.91 cm² total film area, and a 0.015 cm² area was imaged by the microscope camera. Atomic force microscopy (AFM) data was collected using a Horiba LabRam/Aist-NT AFM. Scanning electron microscopy (SEM) image collection was performed using a TESCAN Vega3 SBH with a 5 kV electron beam voltage after sputter-coating with gold.

Spectroscopy. A 1 cm path length quartz cell was used for spectroscopic measurements. An Agilent Varian CARY-60 spectrometer was used to measure the steady state UV–vis absorption. To follow the reaction progress, the azide samples' absorption spectra were recorded in 1 s intervals during exposure to 365 nm light from a AloneFire SV-13 UV light source. The 365 nm light intensity was 9 mW/cm². To induce the formation of aggregates, 65 μ L of a 10⁻² M solution of 2N₃-AN in acetone was added to 4925 μ L of H₂O, resulting in the appearance of a turbid solution.

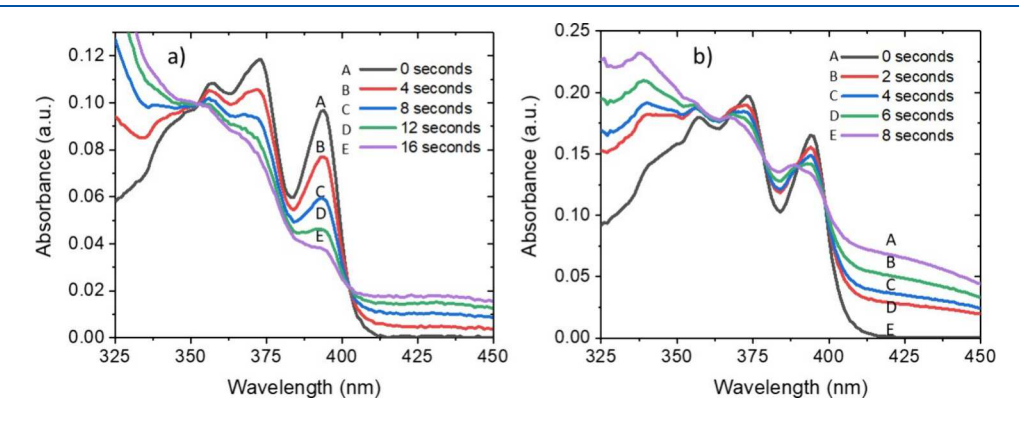


Figure 1. UV—vis absorption spectrum of $2N_3$ -AN irradiated with 365 nm at 9 mW/cm² recorded in (a) chloroform solution where curves A to E show a change in peaks at an interval of 4 s of irradiation starting at t = 0 s and (b) a PMMA polymer film where curves A to E show a change at an interval of 2 s starting at t = 0 s. The decay in the peaks shows photoproduct formation of anthracene nitrene and nitrogen gas.

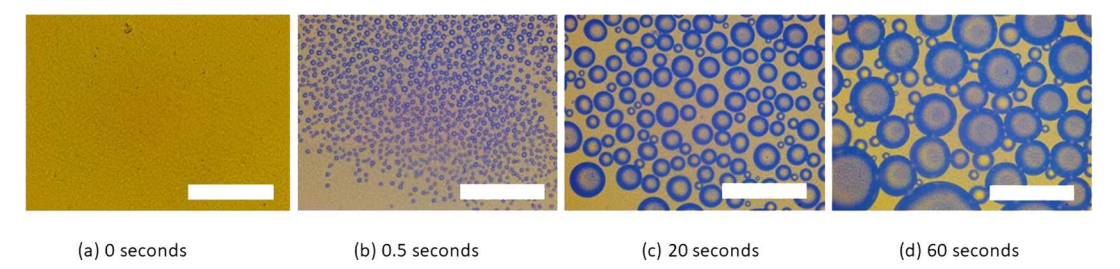


Figure 2. Images of PMMA film doped with $2N_3$ -AN irradiated by 405 nm with an intensity of 149 mW/cm² at various times: (a) 0 s, (b) 0.5 s, (c) 20 s, and (d) 60s. The rapid appearance of small bubbles leads to a coating of bubbles that coalesce into larger bubbles at later times. The scale bar is 100 μ m.

■ RESULTS AND DISCUSSION

The absorption spectrum of $2N_3$ -AN in solution, shown in Figure 1a, resembles that of unsubstituted anthracene but with an additional peak at 394 nm. This red shift likely reflects an inductive effect of the N_3 group conjugated to the aromatic ring. The practical effect is that the absorption is shifted to the near-UV region, making it accessible to 405 nm light from inexpensive diode sources. In solution, excitation at either 365 or 405 nm leads to a rapid decay of the initial absorption peaks and the growth of new, broadened features that extend well into the visible region (Figure 1a). The absorption changes result from the azide photolysis reaction.

The clear isosbestic points observed at 360 and 405 nm are consistent with a single-step photochemical reaction that converts the reactant into product.

We found that 2N₃-AN could be dissolved in PMMA at concentrations of up to 100 mM without detectable aggregation. If 2N₃-AN is reprecipitated into water, the aggregates exhibit a large red shift and absorption line shape change consistent with J-aggregate formation, but the absorption spectra for concentrated PMMA samples were almost identical to those observed in dilute CHCl₃ solution (Figure S10). Air-dried azide-doped and neat PMMA films also exhibited contact angles of 93° and 88°, respectively (Table S2). The presence of 100 mM azide increased the contact angle by $2-5^{\circ}$, which is consistent with the small changes seen for other molecule dopants in organic polymers.^{34,35} If the 2N₃-AN molecules were aggregated at the film surface, we would expect to see larger changes in the absorption spectrum and contact angle. The absence of such changes showed that the azide dopants were homogeneously distributed throughout

When the 2N₃-AN/PMMA films were exposed to UV light, spectral changes similar to those in dilute solutions were observed, as shown in Figure 1b. The nitrene photoproduct has absorption features in the same spectral region as the observed growth in Figure 1,³³ making it the likely origin of the new absorption. However, aromatic nitrenes can subsequently undergo a variety of intramolecular and intermolecular reactions to form more stable species.^{36,37} Using mass spectrometry, we have identified the presence of an azoanthracene dimer and the NO₂ derivative as two products expected from nitrene reactions^{18,19} (Figure S6), but it is possible that others are also formed. Together, these nitrene reaction products give rise to the new absorption features that are seen in Figure 1. In the current work, however, we are

concerned with the dynamics of the N₂ photoproduct whose presence can be inferred from the appearance of gas bubbles.

If a 0.01 M solution of 2N₃-AN in CHCl₃ is illuminated by 365 nm radiation, the solution in the beam path becomes visibly turbid due to the formation of tiny (diameter of <1 mm) N₂ bubbles (Figure S7). This turbidity disappears immediately after the light is removed. This observation suggests that the photolysis reaction in concentrated solution can produce enough N2 molecules to transiently overcome the saturation limit in CHCl₃ and nucleate bubbles.³⁸ Without light exposure, however, these bubbles quickly dissipate as the N₂ molecules dissolve into the surrounding liquid, and the local concentration falls below the saturation limit. In order to create bubbles that persist after removal of light, they must be stabilized somehow. The solubility of N2 in water is approximately 40× lower than in CHCl₃, ³⁹ and water's lower N₂ gas saturation limit and higher surface tension have been shown to facilitate bubble formation.⁴⁰ Unfortunately, 2N₃-AN is insoluble in H2O, which necessitates the use of a heterogeneous solid-liquid interface.

A N₂-producing solid can be created using an air-dried (rough) PMMA film doped with 2N3-AN. When this film is submerged in water and irradiated using either 365 or 405 nm light, rapid bubble evolution on the polymer surface is observed. During the irradiation period, the bubbles steadily grow in diameter and coalesce into larger bubbles as shown in the sequence of images in Figure 2. The bubble radius growth is initially rapid and continues even if the light is turned for a short period (Figure S8) but slows at later times and then occurs only when the light is on, probably as a result of azide concentration depletion. The fact that the bubbles grow even in the absence of light suggests that the N₂ molecules require some time to escape the polymer matrix. Eventually the growth of individual bubbles halts, and further growth only occurs via merging of separate bubbles. Side images of the N2 bubbles on the PMMA surface allowed us to estimate a contact angle in the range of $92 \pm 11^{\circ}$ (Figure S11). This captive bubble angle is within the error range of the sessile drop contact angle measured for the PMMA surface, but it should be noted that it is not necessarily expected to be exactly equal for rough surfaces. 41,42 The relatively high gas bubble contact angle demonstrates that the hydrophobicity of the surface is preserved when submerged in water.

Surprisingly, the layer of surface bubbles was stable for days in water, disappearing only once the polymer film is brought out of the water and exposed to air. The stability of the bubbles is consistent with them containing predominantly N_2 as opposed to water vapor. Previous work has shown that pinning of the water—gas contact line at surface defects can lead to long-lived surface bubbles, 44-46 but other factors such

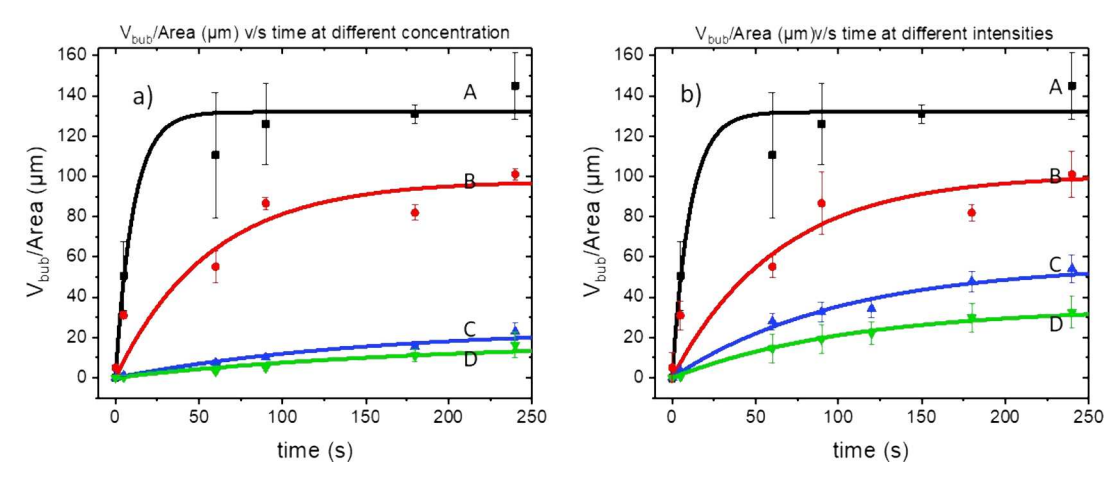


Figure 3. (a) The bubble volume per unit area is plotted versus time for different azide concentrations. The 405 nm light intensity is fixed at 149 mW/cm². The azide concentrations are 0.1 M (A - black squares), 0.07 M (B - red circles M), 0.05 M (C - blue triangles), and 0.03 M (D - green inverted triangles). Also shown are fits to the data using eq 1. (b) The bubble volume per unit area is plotted versus time for different 405 nm light intensities. The azide concentration is fixed at 0.1M. Th light intensities are 145.6 mW/cm² (A - black squares), 44.6 mW/cm² (B - red circles), 15.2 mW/cm² (C - blue triangles), and 4.64 mW/cm² (D - green upside down triangles). Also shown are fits to the data using eq 1. All fit parameters are listed in Table 1.

as the dynamic surface distortion by the bubble itself may also play a role. 47,48 Bubble generation appears to be a general phenomenon and was observed in other azide-doped polymers including polystyrene and polycarbonate.

The appearance of surface bubbles within 1 s of irradiation was surprising. N_2 diffusion in solid polymers is on the order of 10^{-9} cm²/s.^{49,50} At this rate, the time required for a N_2 molecule to traverse half the polymer film thickness (75 μ m) can be estimated to be ~3400 s or several hours. The appearance of surface bubbles within 1 s indicates that N₂ transport is much more rapid than that in neat PMMA under equilibrium conditions. We considered the possibility that azide photolysis inside the polymer may change its porosity to facilitate gas transport. At 0.1 M, the azide molecules are only separated by 2-3 nm, and it is possible that their decomposition frees up the internal volume, which allows the N_2 to flow more easily through the polymer network. Such changes would have to occur on very small length scales since we could not detect any changes in the polymer surface morphology using optical or electron microscopy (Figure S12). Raman spectroscopy provided no evidence for chemical degradation of the PMMA host (Figure S13), but contact angle measurements did show a slight decrease after irradiation (Table S2) possibly due to more polar nitrene side products produced at the surface. Ideally, the gas porosity of freestanding films would be measured before and after irradiation to determine whether photolysis changes the nanoscale connectivity of the polymer host, but such specialized measurements must be reserved for future studies. A second possible explanation for the rapid bubble growth on air-dried films is that the rapid drying leads to greater internal porosity and more rapid gas transport. Again, gas porosity measurements on free-standing films would be useful to assess this possibility. If we assume that photolysis does not change the gas transport properties of the polymer, then a third explanation is that the internal gas pressure drives the newly formed N2 out through the polymer network through normal permeation.⁵¹ The internal pressure generated by the sudden appearance of gas molecules and its effects on transport are not well-studied mainly because there have not been good ways to initiate gas evolution inside a bulk solid at a well-defined point

in time. Whatever its physical origin, rapid transport of the gas to the surface is a necessary condition for bubble growth. Slow arrival of N_2 molecules would never enable the local concentration of N_2 to surpass the saturation limit since diffusion is always moving the N_2 molecules away from the surface into bulk water, where they exist as dissolved gas.

In order to relate the gas evolution to the photochemical reaction kinetics occurring inside the polymer, we calculated the total volume of gas evolved using video analysis to measure the individual bubble radii and then summing up their volumes to calculate the volume of gas evolved per unit area, $\overline{V}_{\mathrm{bub}}$. This approach will underestimate the total amount of N2 produced because some fraction probably remains trapped in the polymer or dissolves into water without being trapped in a bubble. In Figure 3a, we plot the bubble volume per area versus time for several different azide concentrations under the highest 405 nm light intensity, that is, 159 mW/cm². The rate of increase and saturation point both strongly depend on the azide concentration with the lowest concentration yielding almost an order of magnitude fewer bubbles and much slower growth. A strong dependence on the light intensity is also observed (Figure 3b). The growth curves of the areal bubble volume $\overline{V}_{\text{bub}}$ in Figure 3 were fit by assuming exponential growth using the equation

$$\overline{V}_{\text{bub}}(t) = \overline{V}_{\infty}(1 - e^{-k_{\text{bub}}t}) \tag{1}$$

where \overline{V}_{∞} is the asymptotic bubble volume and $k_{\rm bub}$ is the bubble growth rate constant. These fits are overlaid with the data in Figure 3, and the fit parameters \overline{V}_{∞} and $k_{\rm bub}$ are tabulated for the different intensity and azide concentration conditions in Table 1. Equation 1 is not based on a physical model and should be regarded simply as a convenient way to parameterize the data. Equation 1 fits do a fair job of reproducing the data, but the $k_{\rm bub}$ error ranges are on the order of 30% for some of the fits. The error bars in Figure 3 reflect the uncertainty in total volumes measured by our video analysis method (Calculation S3). Bubble formation and growth are stochastic processes, and some variation is probably unavoidable.

Table 1. \overline{V}_{∞} and $k_{\rm bub}$ Tabulated from Fit $\overline{V}_{\rm bub} = \overline{V}_{\infty} (1 - e^{-k_{\rm bub}t})$ for Different Intensities and Concentrations for Air-Dried Rough Films

concentration	\overline{V}_{∞} $(\mu \mathrm{m})$	$k_{\rm bub}~({\rm s}^{-1})$
0.1 M	131 ± 6	$93 \times 10^{-3} \pm 32 \times 10^{-3}$
0.07 M	98 ± 9	$18 \times 10^{-3} \pm 6 \times 10^{-3}$
0.05 M	25 ± 2	$7 \times 10^{-3} \pm 1 \times 10^{-3}$
0.03 M	18 ± 2	$5 \times 10^{-3} \pm 1 \times 10^{-3}$
intensity	$\overline{V}_{\infty}(\mu\mathrm{m})$	$k_{\rm bub}~({\rm s}^{-1})$
145.6 mW/cm^2	126 ± 7	$150 \times 10^{-3} \pm 50 \times 10^{-3}$
44.6 mW/cm^2	100 ± 5	$16 \times 10^{-3} \pm 3 \times 10^{-3}$
15.2 mW/cm^2	56 ± 2	$10 \times 10^{-3} \pm 1 \times 10^{-3}$
	35 + 1	$9.3 \times 10^{-3} + 0.7 \times 10^{-3}$

The data in Figure 3 show that the rate of bubble evolution depends on both the light intensity and azide concentration. This dependence can be understood qualitatively utilizing simple photophysical considerations. If we assume that every photolyzed azide inside the polymer film gives rise to a N_2 molecule at the polymer—water interface, we can estimate the time-dependent N_2 density at the polymer surface, which is denoted $N_{\rm N2}$, using eq 2

$$N_{\rm N2}(t) = C_{\rm Az}^0 (1 - e^{-\sigma I \phi t}) \approx C_{\rm Az}^0 \sigma I \phi t \tag{2}$$

where ϕ is the photolysis quantum yield, I is the intensity, and σ is the absorption cross section. Equation 2 predicts that, at early times, the amount of N2 available for bubble formation should be linearly proportional to the product C_{Az}^0I . It is important to realize that $\overline{V}_{\text{bub}}$ is not just proportional to N_{N2} however. Bubble formation only occurs when the local N₂ density exceeds the saturation limit, so at low C_{Az}^0I values, we would expect to see little bubble formation since N2 diffusion into the bulk water would prevent the local concentration from exceeding this threshold. Based on this physical reasoning, we can expect to see two regimes as we vary I and C_{Az}^0 . The first regime is when most of the surface N2 is lost to diffusion, although there will always be some bubble formation even for small C_{Az}^0I values due to surface sites that are very favorable for nucleation. The second regime is when the rate of surface N₂ production exceeds the diffusive loss, and the local concentration surpasses the saturation limit. At this point, we expect to see the bubble growth accelerate but remain linear with C_{Az}^0I . In Figure 4, the plot of k_{bub} versus C_{Az}^0I does indeed exhibit the predicted two stage behavior with a threshold of $C_{Az}^{0}I$ of ~10 M·mW/cm² after which bubble growth rapidly increases. A quantitative description of the bubble evolution will require a more detailed characterization of the polymer surface as well as modeling the bubble nucleation and growth, which is similar to what is done to model bubble growth on plasmonic particles⁵² and electrode surfaces.^{53,54} Nevertheless, our simple analysis provides at least a qualitative starting point for further study of this phenomenon.

The bubble dynamics were sensitive to the surface morphology of the PMMA films. When a freshly cast film was left to dry in the open air, we found that the surface exhibited features densely arrayed across the surface, as shown in the SEM image in Figure 5a. These surface features gave rise to a hazy appearance upon optical examination. Previous work has shown that the surface roughness of a spin-coated polymer film is very sensitive to the evaporation rate, ^{55,56} and that this roughness can be controlled to some extent. ⁵⁷ To prepare

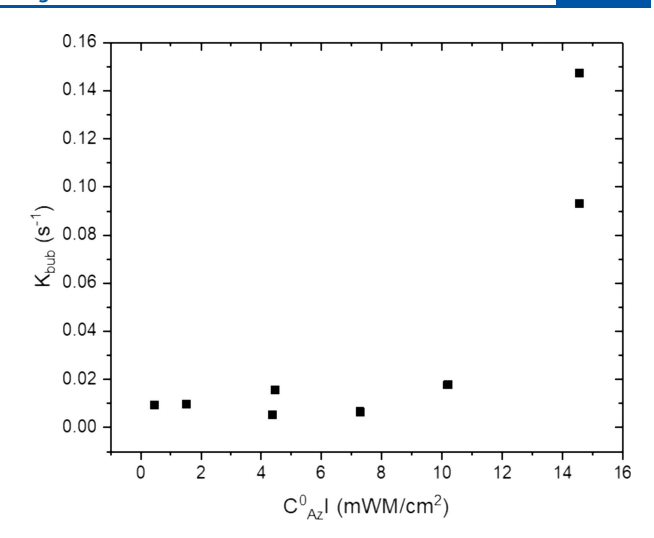


Figure 4. Rate of bubble formation k_{bub} plotted against the product $C_{\Delta x}^0 I$. The rate of bubble formation increases dramatically at around $C_{\Delta x}^0 I = 10 \text{ M mW/cm}^2$, which corresponds to a threshold for bubble nucleation at the surface.

smooth films with high optical clarity, freshly cast films were placed in a closed container to slow solvent evaporation and eliminate air currents. These films did not exhibit random surface eruptions, as shown in Figure 5c and were optically clear. A comparison of the surface profiles measured using AFM is shown in Figure 5b-d. The rough air-dried film has 200 nm tall features that are several microns in diameter, while the smooth film has much smaller features that are less effective for bubble nucleation. This can be seen from a comparison of the bubble production of the two film morphologies (Figure 6). Fitting the data using eq 1, we found that the smooth film had a \overline{V}_{∞} = 33 μ m, which is approximately $4\times$ less than that of the rough film, while its k_{bub} $= 8 \times 10^{-3} \text{ s}^{-1}$ was approximately 15× smaller than that of the rough film. The enhanced bubble formation observed on rough PMMA surfaces likely results from their increased hydrophobicity⁵⁸ (as evidenced by their higher contact angles in Table S2) that facilitates the displacement of water and the association of hydrophobic N_2 . Experimentally, the ability of textured surfaces to catalyze bubble formation is wellestablished. 60,61 Starting with the smooth films, we tried several different methods to roughen their surfaces, including abrasion using sandpaper or sandblasting, but the air-dried films always gave superior performance; therefore, unless otherwise noted, all results in this paper were obtained using the air-dried films.

For practical applications, we were interested in the total bubble yield. Given $C_{\rm Az}^0=0.1$ M and a 150 μ m-thick film, we can calculate a maximum areal density of bubbles, assuming that 100% of the azides react¹⁷ and 100% of the N_2 molecules become trapped in bubbles, of $\bar{V}_{\infty}=366~\mu{\rm m}^3/\mu{\rm m}^2=366~\mu{\rm m}$ (eq S1). From the data in Table 1 for the air-dried PMMA films, we measure an areal density of $\bar{V}_{\infty}=145~\mu{\rm m}$, corresponding to a 40% yield. This value suggests that the rough films can effectively trap gas at the surface, but improved surface texturing or a secondary coating might increase the yield of trapped gas by a factor of 2.5.

The ability of the bubbles to remain stably attached to the polymer surface means that they form a single mechanical object. The nominal density of solid PMMA is 1.1 g/cm³ and is higher than that of H₂O, causing the PMMA to sink to the

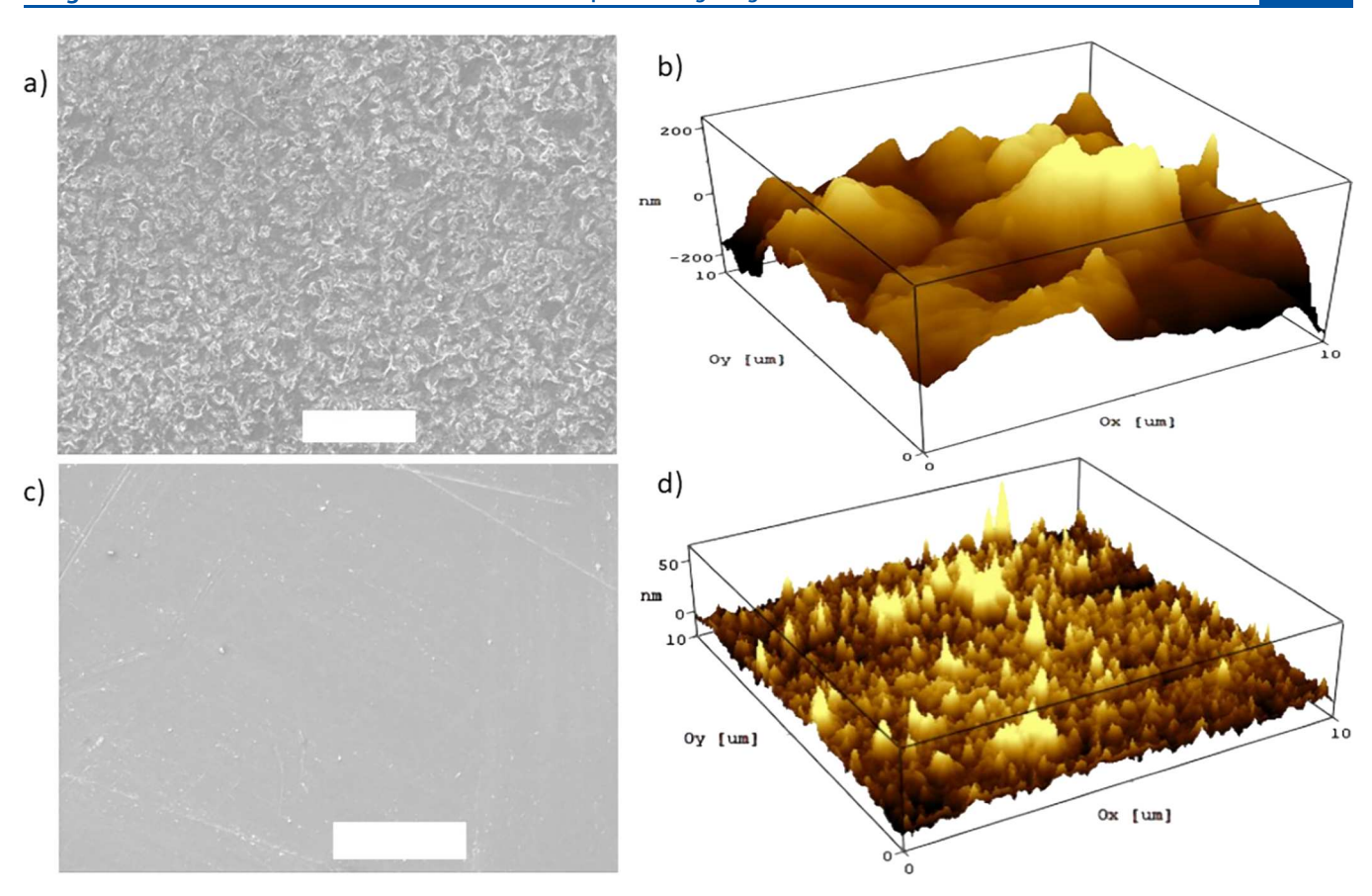


Figure 5. (a) SEM images of the PMMA film with 0.1 M azide dried in open air, resulting in a rough film, and (b) AFM images with the same rough film showing fewer peaks and valleys with a dynamic range between 50 to 200 nm. (c) SEM images of the PMMA film dried in a closed container, resulting in a smooth film. (d) AFM images of the smooth PMMA film with multiple peaks and valleys of a 10 nm range surface roughness.

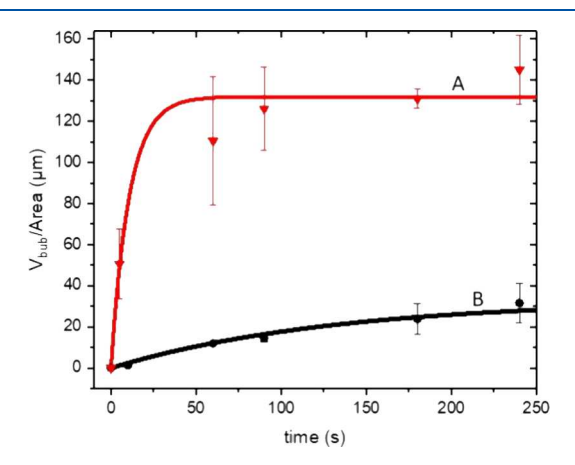


Figure 6. Exponential plot of the areal bubble volume for smooth (B -black) and rough films (A - red) and fits using eq 1. The rough film's \bar{V}_{∞} is four times larger than that of the smooth film, and $k_{\rm bub}$ is 16 times larger.

bottom of the transparent container in Figure 7a. After photolysis and bubble formation, the density of the polymer—bubble composite structure will be lower, allowing the film coated with bubbles to float to the water surface, as shown in Figure 7b—d. It is straightforward to show that the density of the polymer film plus attached bubble layer is given by (eq S2)

$$\rho = \rho_0 \frac{d}{d + \overline{V}_{\infty}} \tag{3}$$

where d is the film thickness and ρ_0 is the density of the polymer film before bubble formation. Using eq 3 and $\overline{V}_{\infty}=145~\mu\text{m}$, we calculate a density of $\rho=0.6~\text{g/cm}^3$ after photolysis and bubble formation, which is sufficient to float the bubble-coated film, as observed. It is important to note that flotation relies on the adhesion of the N_2 bubbles to the polymer surface being stronger than gravitational and Brownian forces, which would cause them to detach and float to the surface individually.

The ability to create persistent surface bubbles using photochemistry also provides a new method for the creation of stable bubble arrays. Photothermal patterning provides a way to create vapor bubbles across an absorbing surface, but these bubbles tend to recondense into the liquid phase. 62,63 Figure 8 shows some examples of controlled pattern formation by using a focused laser that is scanned across the sample. Bubbles are formed along the laser track accompanied by a brown discoloration due to the photoproducts. The square pattern shown in Figure 8 was created by scanning a 405 nm laser beam with a power of 10 mW and a spot diameter of $100~\mu m$. This method begins with a homogeneous surface that can be patterned in an arbitrary way in contrast to physical or chemical surface patterning 64,65 that requires the bubble pattern to be determined in advance. It also does not

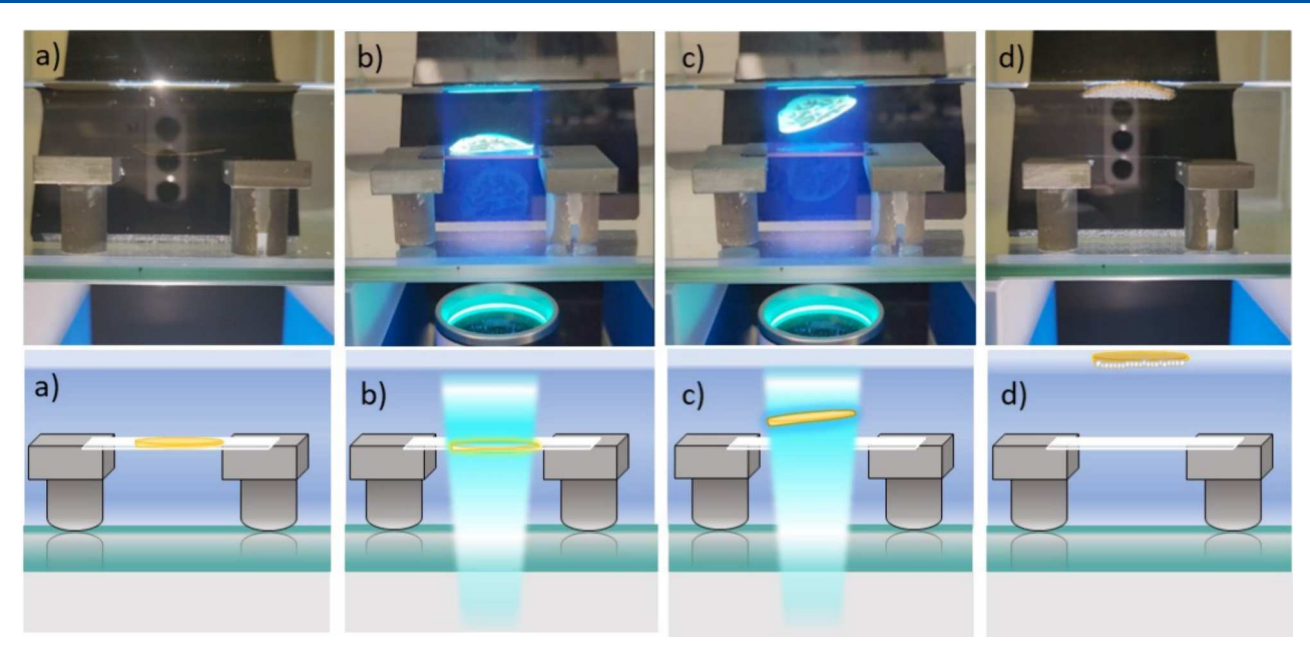


Figure 7. A 2.5 cm diameter PMMA film doped with 0.1 M azide rests on a glass slide suspended between two metal pillars and exposed to 365 nm light. (a) Before irradiation; (b) after 8 min, the film bends but still rests on the slide; (c) after 8.2 min, the film floats to the surface; and (d) after 8 h with the light turned off, the film remains floating. The top row of images are photographs, while the bottom row illustrates what is going on with the film during irradiation. The film covered with bubbles stays afloat for longer than three days when left undisturbed.

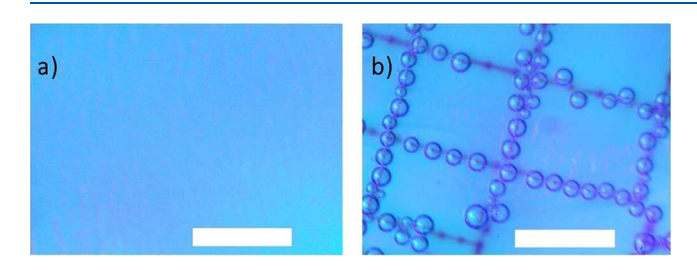


Figure 8. Patterning on a PMMA polymer film doped with 0.1 M azide using a focused 405 nm laser. The images show (a) the PMMA film before patterning and (b) the PMMA surface after scanning the laser spot across the sample in a square grid pattern. The scale bar is $100~\mu m$.

require physical contact with the substrate in contrast with tribonucleation. 66

CONCLUSIONS

The results in this paper demonstrate that molecular photochemistry can be harnessed to produce gas bubbles from a solid-state sample. Azide photolysis in a PMMA solid film can generate a stable layer of bubbles with a yield of gas on the order of 40%. The remarkable property that enables the high amount of bubble formation appears to be the rapid transport of the N2 photoproduct through the polymer to the surface, which is not well-understood at the present time. The spatial selectivity enabled by the use of light allows the creation of complex spatial patterns, while the gas trapped in the adhered bubbles can enable the polymer film to float to the surface. Photoinduced bubble formation may provide a useful way to switch material properties, such as buoyancy, acoustic wave propagation, and thermal conductivity. The use of light to initiate gas evolution from a solid illustrates how molecular photochemistry can provide the basis for new classes of stimuli-responsive materials.

ASSOCIATED CONTENT

Supporting Information

The Supporting Information is available free of charge at https://pubs.acs.org/doi/10.1021/acs.langmuir.3c02869.

Additional experimental details including descriptions of the synthesis of the azidoanthracene and its characterization, polymer sample preparation and characterization, data analysis methods for bubble gas evolution, contact angle measurements, and Raman spectroscopy (PDF)

AUTHOR INFORMATION

Corresponding Author

Christopher J. Bardeen — Department of Chemistry, University of California, Riverside, Riverside, California 92521, United States; orcid.org/0000-0002-5755-9476; Email: christopher.bardeen@ucr.edu

Authors

Pranaya P. Ghate – Department of Chemical and Environmental Engineering, University of California, Riverside, Riverside, California 92521, United States

Kerry M. Hanson − Department of Chemistry, University of California, Riverside, Riverside, California 92521, United States; occid.org/0000-0002-6942-3330

Kevin Lam − Department of Chemistry, University of California, Riverside, Riverside, California 92521, United States; occid.org/0009-0007-6606-8170

Rabih O. Al-Kaysi — College of Science and Health Professions-3124, King Saud bin Abdulaziz University for Health Sciences, and King Abdullah International Medical Research Center (Nanomedicine), Ministry of National Guard Health Affairs, Riyadh 11426, Kingdom of Saudi Arabia; orcid.org/0000-0001-8429-2802

Complete contact information is available at: https://pubs.acs.org/10.1021/acs.langmuir.3c02869

Notes

The authors declare no competing financial interest.

ACKNOWLEDGMENTS

This work was supported by the Office of Naval Research through the MURI on Photomechanical Material Systems (no. ONR N00014-18-1-2624) and the National Science Foundation, no. DMR-1810514.

REFERENCES

- (1) Hoffman, A. S. Stimuli-responsive polymers: Biomedical applications and challenges for clinical translation. *Adv. Drug Delivery Rev.* **2013**, *65*, 10–16.
- (2) Wei, M.; Gao, Y.; Li, X.; Serpe, M. J. Stimuli-responsive polymers and their applications. *Polym. Chem.* **2017**, *8*, 127–143.
- (3) Zhao, Y.; Hua, M.; Yan, Y.; Wu, S.; Alsaid, Y.; He, X. Stimuli-Responsive Polymers for Soft Robotics. *Annu. Rev. Control Robot. Auton. Syst.* **2022**, *5*, 515–545.
- (4) Ikeda, T.; Mamiya, J.-i.; Yu, Y. Photomechanics of Liquid-Crystalline Elastomers and Other Polymers. *Angew. Chem., Int. Ed.* **2007**, *46*, 506–528.
- (5) White, T. J.; Broer, D. J. Programmable and adaptive mechanics with liquid crystal polymer networks and elastomers. *Nat. Mater.* **2015**, *14*, 1087–1098.
- (6) Gerkman, M. A.; Gibson, R. S. L.; Calbo, J.; Shi, Y.; Fuchter, M. J.; Han, G. G. D. Arylazopyrazoles for Long-Term Thermal Energy Storage and Optically Triggered Heat Release below 0 °C. *J. Am. Chem. Soc.* **2020**, *142*, 8688–8695.
- (7) Liu, K.; Cheng, C.; Cheng, Z.; Wang, K.; Ramesh, R.; Wu, J. Giant-Amplitude, High-Work Density Microactuators with Phase Transition Activated Nanolayer Bimorphs. *Nano Lett.* **2012**, *12*, 6302–6308.
- (8) Lui, B. F.; Bardeen, C. J. Using Small Molecule Absorbers to Create a Photothermal Wax Motor. *Small* **2022**, *18*, 2105356.
- (9) Xu, W.-C.; Sun, S.; Wu, S. Photoinduced Reversible Solid-to-Liquid Transitions for Photoswitchable Materials. *Angew. Chem., Int. Ed.* **2019**, *58*, 9712–9740.
- (10) Miriyev, A.; Stack, K.; Lipson, H. Soft material for soft actuators. *Nat. Commun.* 2017, 8, 596.
- (11) Noguchi, T.; Tsumori, F. Soft actuator with large volumetric change using vapor—liquid phase transition. *Jpn. J. Appl. Phys.* **2020**, 59, SIIL08.
- (12) Li, X.; Duan, H.; Lv, P.; Yi, X. Soft Actuators Based on Liquid–Vapor Phase Change Composites. *Soft Robotics* **2021**, *8*, 251–261.
- (13) Chellattoan, R.; Yudhanto, A.; Lubineau, G. Low-Voltage-Driven Large-Amplitude Soft Actuators Based on Phase Transition. *Soft Robotics* **2020**, *7*, 688–699.
- (14) Halford, B. What chemicals make airbags inflate, and how have they changed over time? Chem. Eng. News2022.
- (15) Turro, N. J. Modern Molecular Photochemistry; University Science Books: Sausalito, CA, 1991.
- (16) Chung, T. S.; Lopez, S. A.; Houk, K. N.; Garcia-Garibay, M. A. Stereospecific Synthesis of Substituted Aziridines by a Crystal-to-Crystal Photodenitrogenation of Δ^2 -1,2,3-Triazolines. *Org. Lett.* **2015**, 17, 4568–4571.
- (17) Reiser, A.; Marley, R. Photolysis of Aromatic Azides Part 3.-Quantum Yield and Mechanism. *Trans. Faraday Soc.* **1968**, *64*, 1806–1815.
- (18) Gritsan, N. P.; Pritchina, E. A. The mechanism of photolysis of aromatic azides. Russ. Chem. Rev. 1992, 61, 910-939.
- (19) Schuster, G. B.; Platz, M. S. Photochemistry of Phenyl Azide. Adv. Photochem. 1992, 17, 69–143.
- (20) Gritsan, N. P.; Platz, M. S. Kinetics, Spectroscopy, and Computational Chemistry of Arylnitrenes. *Chem. Rev.* **2006**, *106*, 3844–3867.
- (21) Shields, D. J.; Karothu, D. P.; Sambath, K.; Ranaweera, R. A. A. U.; Schramm, S.; Duncan, A.; Duncan, B.; Krause, J. A.; Gudmundsdottir, A. D.; Naumov, P. e. Cracking under Internal

- Pressure: Photodynamic Behavior of Vinyl Azide Crystals through N_2 Release. J. Am. Chem. Soc. **2020**, 142, 18565–18575.
- (22) McCormick, M. E.; Bhattachayra, R. Drag Reduction of a Submersible Hull by Electroysis. *Naval. Eng. J.* **1973**, *85*, 11–16.
- (23) Murai, Y. Frictional drag reduction by bubble injection. *Exp. Fluids* **2014**, *SS*, 1773.
- (24) Sharma, G. S.; Skvortsov, A.; MacGillivray, I.; Kessissoglou, N. Sound scattering by a bubble metasurface. *Phys. Rev. B* **2020**, *102*, No. 214308.
- (25) Huang, Z.; Zhao, S.; Su, M.; Yang, Q.; Li, Z.; Cai, Z.; Zhao, H.; Hu, X.; Zhou, H.; Li, F.; Yang, J.; Wang, Y.; Song, Y. Bioinspired Patterned Bubbles for Broad and Low-Frequency Acoustic Blocking. ACS Appl. Mater. Interfaces 2020, 12, 1757–1764.
- (26) Goyal, R.; Athanassiadis, A. G.; Ma, Z.; Fischer, P. Amplification of Acoustic Forces Using Microbubble Arrays Enables Manipulation of Centimeter-Scale Objects. *Phys. Rev. Lett.* **2022**, *128*, No. 254502.
- (27) Ferrara, K.; Pollard, R.; Borden, M. Ultrasound Microbubble Contrast Agents: Fundamentals and Application to Gene and Drug Delivery. *Annu. Rev. Biomed. Engin.* **2007**, *9*, 415–447.
- (28) Jia, P.; Chen, W.; Qiao, J.; Zhang, M.; Zheng, X.; Xue, Z.; Liang, R.; Tian, C.; He, L.; Di, Z.; Wang, X. Programmable graphene nanobubbles with threefold symmetric pseudo-magnetic fields. *Nat. Commun.* **2019**, *10*, 3127.
- (29) Liang, X.; Kumar, V.; Ahmadi, F.; Zhu, Y. Manipulation of droplets and bubbles for thermal applications. *Droplet* **2022**, *1*, 80–
- (30) Fauria, K. E.; Manga, M.; We, Z. Trapped bubbles keep pumice afloat and gas diffusion makes pumice sink. *Earth Planet. Sci. Lett.* **2017**, *460*, 50–59.
- (31) Biswas, B.; Venkateswarulu, M.; Gaur, P.; Sharma, Y.; Sinha, S.; Ghosh, S. Triggered emission for rapid detection of hydrogen sulfide chaperoned by large Stokes shift. *J. Photochem. Photobiol., A* **2019**, 371, 264–270.
- (32) Reiser, A.; Bowes, G.; Horne, R. J. Photolysis of Aromatic Azides. Part 1. Electronic Spectra of Aromatic Nitrenes and their Parent Azides. *Trans. Faraday Soc.* **1966**, *62*, 3162–3169.
- (33) Alvarado, R.; Grivet, J.-P.; Igier, C.; Barcelo, J.; Rigaudy, J. Spectroscopic studies of azides and nitrenes derived from anthracene. *J. Chem. Soc., Faraday Trans.* **1977**, 2 (73), 844–857.
- (34) Athanassiou, A.; Lygeraki, M. I.; Pisignano, D.; Lakiotaki, K.; Varda, M.; Mele, E.; Fotakis, C.; Cingolani, R.; Anastasiadis, S. H. Photocontrolled Variations in the Wetting Capability of Photochromic Polymers Enhanced by Surface Nanostructuring. *Langmuir* **2006**, 22, 2329–2333.
- (35) Mostafavi, S. H.; Tong, F.; Dugger, T. W.; Kisailus, D.; Bardeen, C. J. Noncovalent Photochromic Polymer Adhesion. *Macromolecules* **2018**, *51*, 2388–2394.
- (36) Wentrup, C. Nitrenes, Carbenes, Diradicals, and Ylides. Interconversions of Reactive Intermediates. *Acc. Chem. Res.* **2011**, 44, 393–404.
- (37) Sankaranarayanan, J.; Rajam, S.; Hadad, C. M.; Gudmundsdottir, A. D. The ability of triplet nitrenes to abstract hydrogen atoms. *J. Phys. Org. Chem.* **2010**, 23, 370–375.
- (38) Maloth, R. K. N.; Khayat, R. E.; DeGroot, C. T. Bubble Growth in Supersaturated Liquids. *Fluids* **2022**, *7*, 365.
- (39) Battino, R.; Rettich, T. R.; Tominaga, T. The Solubility of Nitrogen and Air in Liquids. *J. Phys. Chem. Ref. Data* **1984**, *13*, 563–600.
- (40) Rubin, M. B.; Noyes, R. M. Thresholds for nucleation of bubbles of nitrogen in various solvents. *J. Phys. Chem.* **1992**, *96*, 993–1000
- (41) Drelich, J.; Miller, J. D.; Good, R. J. The Effect of Drop (Bubble) Size on Advancing and Receding Contact Angles for Heterogeneous and Rough Solid Surfaces as Observed with Sessile-Drop and Captive-Bubble Techniques. *J. Colloid Interface Sci.* **1996**, 179, 37–50.
- (42) Ruiz-Cabello, F. J. M.; Rodríguez-Valverde, M. A.; Marmur, A.; Cabrerizo-Vílchez, M. A. Comparison of Sessile Drop and Captive

- Bubble Methods on Rough Homogeneous Surfaces: A Numerical Study. *Langmuir* **2011**, 27, 9638–9643.
- (43) Baffou, G.; Polleux, J.; Rigneault, H.; Monneret, S. Super-Heating and Micro-Bubble Generation around Plasmonic Nanoparticles under cw Illumination. *J. Phys. Chem. C* **2014**, *118*, 4890–4898.
- (44) Liu, Y.; Zhang, X. Nanobubble stability induced by contact line pinning. *J. Chem. Phys.* **2013**, *138*, No. 014706.
- (45) Zhang, X.; Chan, D. Y. C.; Wang, D.; Maeda, N. Stability of Interfacial Nanobubbles. *Langmuir* 2013, 29, 1017–1023.
- (46) Lohse, D.; Zhang, X. Pinning and gas oversaturation imply stable single surface nanobubbles. *Phys. Rev. E* **2015**, *91*, No. 031003.
- (47) Guo, Z.; Wang, X.; Zhang, X. Stability of Surface Nanobubbles without Contact Line Pinning. *Langmuir* **2019**, *35*, 8482–8489.
- (48) Qian, J.; Craig, V. S. J.; Jehannin, M. Long-Term Stability of Surface Nanobubbles in Undersaturated Aqueous Solution. *Langmuir* **2019**, 35, 718–728.
- (49) Patel, V. M.; Patel, C. K.; Patel, K. C.; Patel, R. D. Diffusion of gases in poly(methyl methacrylate). *Makromol. Chem.* 1972, 158, 65.
- (50) Haraya, K.; Hwang, S.-T. Permeation of oxygen, argon and nitrogen through polymer membranes. *J. Membr. Sci.* **1992**, *71*, 13–27
- (51) Islam, M. A.; Buschatz, H. Gas permeation through a glassy polymer membrane: chemical potential gradient or dual mobility mode? *Chem. Eng. Sci.* **2002**, *57*, 2089–2099.
- (52) Metwally, K.; Mensah, S.; Baffou, G. Fluence Threshold for Photothermal Bubble Generation Using Plasmonic Nanoparticles. *J. Phys. Chem. C* **2015**, *119*, 28586–28596.
- (53) Taqieddin, A.; Nazari, R.; Rajic, L.; Alshawabkeh, A. Review—Physicochemical Hydrodynamics of Gas Bubbles in Two Phase Electrochemical Systems. *J. Electrochem. Soc.* **2017**, *164*, E448–E459.
- (54) Ma, Y.; Guo, Z.; Chen, Q.; Zhang, X. Dynamic Equilibrium Model for Surface Nanobubbles in Electrochemistry. *Langmuir* **2021**, 37, 2771–2779.
- (55) Strawhecker, K. E.; Kumar, S. K.; Douglas, J. F.; Karim, A. The Critical Role of Solvent Evaporation on the Roughness of Spin-Cast Polymer Films. *Macromolecules* **2001**, *34*, 4669–4672.
- (56) Chapman, N.; Chapman, M.; Euler, W. B. Evolution of Surface Morphology of Spin-Coated Poly(Methyl Methacrylate) Thin Films. *Polymers* **2021**, *13*, 2184.
- (57) Mokarian-Tabari, P.; Geoghegan, M.; Howse, J. R.; Heriot, S. Y.; Thompson, R. L.; Jones, R. A. L. Quantitative evaluation of evaporation rate during spin-coating of polymer blend films: Control of film structure through defined-atmosphere solvent-casting. *Eur. Phys. J. E* **2010**, 33, 283–289.
- (58) Accardo, A.; Gentile, F.; Mecarini, F.; De Angelis, F.; Burghammer, M.; Di Fabrizio, E.; Riekel, C. Ultrahydrophobic PMMA micro- and nano-textured surfaces fabricated by optical lithography and plasma etching for X-ray diffraction studies. *Microelectron. Eng.* **2011**, *88*, 1660–1663.
- (59) Li, W.; Zuo, X.; Zhou, X.; Lu, H. Effect of aggregated gas molecules on dewetting transition of water between nanoscale hydrophobic plates. *J. Chem. Phys.* **2019**, *150*, 104702.
- (60) Pinchasik, B.-E.; Schönfeld, F.; Kappl, M.; Butt, H.-J. Bubbles nucleating on superhydrophobic micropillar arrays under flow. *Soft Matter* **2019**, *15*, 8175–8183.
- (61) Deng, X.; Shan, Y.; Meng, X.; Yu, Z.; Lu, X.; Ma, Y.; Zhao, J.; Qiu, D.; Zhang, X.; Liu, Y.; Chen, Q. Direct measuring of single—heterogeneous bubble nucleation mediated by surface topology. *Proc. Natl. Acad. Sci.* **2022**, *119*, No. e2205827119.
- (62) Li, J.; Zhao, F.; Deng, Y.; Liu, D.; Chen, C.-H.; Shih, W.-C. Photothermal generation of programmable microbubble array on nanoporous gold disks. *Opt. Express* **2018**, *26*, 16893.
- (63) Ohannesian, N.; Li, J.; Misbah, I.; Zhao, F.; Shih, W.-C. Directed Concentrating of Micro-/Nanoparticles via Near-Infrared Laser Generated Plasmonic Microbubbles. *ACS Omega* **2020**, *5*, 32481–32489.
- (64) Perez-Toralla, K.; Konda, A.; Bowen, J. J.; Jennings, E. E.; Argyropoulos, C.; Morin, S. A. Rational Synthesis of Large-Area

- Periodic Chemical Gradients for the Manipulation of Liquid Droplets and Gas Bubbles. *Adv. Funct. Mater.* **2018**, *18*, 1705564.
- (65) Choi, C.-H.; David, M.; Gao, Z.; Chang, A.; Allen, M.; Wang, H.; Chang, C.-h Large-scale Generation of Patterned Bubble Arrays on Printed Bi-functional Boiling Surfaces. *Sci. Rep.* **2016**, *6*, 23760.
- (66) Wildeman, S.; Lhuissier, H.; Sun, C.; Lohse, D.; Prosperetti, A. Tribonucleation of bubbles. *Proc. Natl. Acad. Sci.* **2014**, *111*, 10089–10094.